remote sensing

MDPI

Article

Spatio-Temporal Validation of GNSS-Derived Global Ionosphere Maps Using 16 Years of Jason Satellites Observations

Mateusz Poniatowski [1,2,*], Grzegorz Nykiel [2,3], Claudia Borries [4] and Jędrzej Szmytkowski [1]

[1] Faculty of Applied Physics and Mathematics, Gdańsk University of Technology, 80-233 Gdańsk, Poland
[2] Digital Technologies Center, Gdańsk University of Technology, 80-233 Gdańsk, Poland
[3] Faculty of Civil and Environmental Engineering, Gdańsk University of Technology, 80-233 Gdańsk, Poland
[4] German Aerospace Center, DLR, Institute for Solar-Terrestrial Physics, 17235 Neustrelitz, Germany
* Correspondence: mateusz.poniatowski@pg.edu.pl

Abstract: Existing ionospheric models perform very well in mapping the calm state of the ionosphere. However, the problem is accurately determining the total electron content (TEC) for disturbed days. Knowledge of the exact electron density is essential for single−frequency receivers, which cannot eliminate the ionospheric delay. This study aims to investigate temporal and spatial variability in the distribution of TEC based on differences between maps of individual Ionospheric Associated Analysis Centers (IAACs) of the International GNSS Service (IGS) and aligned altimetry−TEC from 2005–2021. Based on the temporal distribution, we have observed a significant effect of solar activity on the mean and standard deviation behavior of the differences between global ionospheric maps (GIMs) and Jason−derived TEC. We determined the biases for the entire calculation period, through which it can be concluded that the upcg-Jason and igsg-Jason differences have the lowest standard deviation (±1.81 TECU). In addition, the temporal analysis made it possible to detect annual, semi−annual, and 117-day oscillations occurring in the Jason−TEC data, as well as 121-day oscillations in the GIMs. It also allowed us to analyze the potential sources of these cyclicities, solar and geomagnetic activity, in the case of the annual and semi−annual periodicities. When considering spatial variations, we have observed that the most significant average differences are in the intertropical areas. In contrast, the smallest differences were recorded in the southern hemisphere, below the Tropic of Capricorn (23.5°S). However, the slightest variations were noted for the northern hemisphere above the Tropic of Cancer (23.5°N). Our research presented in this paper allows a better understanding of how different methods of GNSS TEC approximation affect the model's accuracy.

Keywords: GIMs; ionospheric models; TEC; GNSS; altimetry; oscillations

Citation: Poniatowski, M.; Nykiel, G.; Borries, C.; Szmytkowski, J. Spatio-Temporal Validation of GNSS-Derived Global Ionosphere Maps Using 16 Years of Jason Satellites Observations. *Remote Sens.* **2023**, *15*, 5053. https://doi.org/10.3390/rs15205053

Academic Editors: Shuanggen Jin, Mariusz Specht and Gino Dardanelli

Received: 6 September 2023
Revised: 14 October 2023
Accepted: 19 October 2023
Published: 21 October 2023

1. Introduction

The ionosphere is a heterogeneous atmospheric layer exposed to intense solar radiation [1], in which ionization and recombination processes cause a continuous electron density variation in different ionosphere regions. Its inhomogeneous nature is one of the causes of propagation disturbances to signals passing through it [2]. It causes wave rotation, known as Faraday rotation, and group delay, which has the most significant effect on code measurements by delaying them, along with the acceleration of phase measurements and wave dispersion. The interference associated with the continuous electron density variation along the signal path is mostly eliminated using dual−frequency measurements, reducing the impact of the first−order ionospheric term [3]. However, when performing single−frequency measurements, it is impossible to obtain a direct value of the delay from the information contained in the signal. The knowledge of the electron density in the signal path is essential for single−frequency measurements [4], where models such as NeQuick2 [5] or International Reference Ionosphere (IRI) [6] have been developed to

consider the ionospheric correction for single−frequency measurements. The main purpose of creating these models is to represent the state of the ionosphere and its monitoring, along with the acquisition of valuable information that improves the quality of pseudo−distance determination. These models show very good performance for the calm state of the ionosphere. However, when disturbances occur that lead to changes in the electron density distribution, the accuracy and reliability of measurements based on these models decrease. The causes of the major disturbances of the ionosphere are coronal mass ejections from the Sun [7–9], which causes sudden changes in the structure of the ionosphere, resulting in significant measurement errors that are hard to eliminate. Especially rapid and large total electron content (TEC) variations can cause a significant decrease in the accuracy and reliability of GNSS positioning [10–12]. Measurements on two frequencies allow the use of a geometry−free linear combination [13] to determine the slant TEC on the satellite−receiver signal path. The slant TEC values can then be converted into the vertical direction. Thanks to that, it has been possible to study the ionospheric state using GNSS technology on the regional [14] and global scale [15] in real−time [16] or in post−process [17]. GNSS−derived TEC can also investigate traveling ionospheric disturbances [18,19] or estimate ionospheric perturbations generated by natural hazards [20]. One of the utilizations of GNSS TEC is to create global ionospheric maps (GIMs) using ground−based reference stations working in the International GNSS Service (IGS) network. The IGS also provides GIMs: rapid products updated daily with 11−hour latency and final updates weekly with 11-day latency. IGS products are combined based on the individual results provided by research centers called Ionosphere Associate Analysis Centers (IAACs), which are the Center for Orbit Determination in Europe (CODE) [21], European Space Agency (ESA) [22], Jet Propulsion Laboratory (JPL) [23], Polytechnic University of Catalonia (UPC) [24], Wuhan University (WHU) [25], Chinese Academy of Science (CAS) [26], and Natural Resources Canada (NRCan) [27]. The IAACs deliver their solution to the IGS, which combines them to create a final product [28]. As with any model, its accuracy and reliability should be checked. In the case of GIM, there are several possible approaches: assessment of the consistency between models from different IAACs, validation using GNSS−derived TEC or using altimetry satellite measurements, and evaluation of the single−frequency GNSS positioning accuracy. All these approaches have been the subject of recent studies. Wielgosz [29] assessed the quality of the different GIMs in 2014 and 2018, where solar activity was low and high, respectively, using both altimetry and GPS data. They noticed a high agreement between different GIMs and that the accuracy of TEC decreases with decreasing latitude. The same conclusion was observed in similar previous works [30]. Roma−Dollase [31] also found that the new IAAC provides GIMs within accuracy limits set by the other centers. Other studies confirm that the ionospheric maps obtained by processing GNSS data within the IGS framework give a better solution than the data from the IRI model [32], and that the CODE model performs best, obtaining the lowest mean errors [33,34]. Since the TOPEX mission began, it has become possible to determine TEC values using a dual−frequency altimeter [35]. Like TOPEX/Poseidon, the Jason mission, which has been providing altimetry information since late 2001, is used to study the ionosphere. This data has been used as a reference for any ionospheric−related models. For instance, data derived from the altimetric missions were used to validate the IRI−2016 and NeQuick2 models [36]. The obtained biases were between −5.0 and 0 TECU and between 2.5 and 7.5 TECU compared to Jason−2- and Jason−3-derived TEC, respectively. In addition, the same biases against the IGS product were between 2.0 and 6.0 TECU and between 4.0 and 7.0 TECU. More detailed studies of comparison GIMs from different IAAC with Jason−derived TEC were performed by Wielgosz [29]. They obtained values from 0 to 2.14 TECU when they corrected Jason's data by electron content in the plasmasphere. Also, Chen [33] examined the bias between IAAC centers and TEC derived from Jason−2 data, and they obtained low mean values (−1.34 to 0.93 TECU) along with a low standard deviation (from ±1.42 to ±2.46 TECU).

This work aimed to detect and analyze the long−term differences between TEC derived from selected IAAC GIMs and Jason−derived TEC. This paper presents the mag-

nitude and variations of TEC differences and their changes with solar and geomagnetic activity. We also show the spectral analysis and discuss the potential sources of the existing oscillations. Our results allow us to better understand how different GIM modeling impacts TEC values, their spatiotemporal distribution, and variability.

2. Materials and Methods

Based on dual−frequency measurements from GNSS reference stations, the IAACs generate GIMs [37] as a regular grid with 2-h temporal and 2.5° (latitude) × 5.0° (longitude) spatial resolution. These maps are stored in the IONosphere Map Exchange Format Version (IONEX) format, which allows for standardizing the presentation of the TEC data received from individual analysis centers and from which the final IGS product is derived and stored in the same format. An original approach characterizes each model using different methods and assumptions. In this section, we briefly describe the methodology of each IAAC. We also provide detailed information about Jason−derived TEC.

2.1. GIM Models

2.1.1. Center for Orbit Determination in Europe (CODE)

This model assumes a modified single−layer structure of the ionosphere [38], where all electrons are contained in a shell of an infinitesimal thickness [21], together with the use of a basic mapping function. The solution is based on a spherical function of degree 15, which can be written in the form:

$$TEC(\varphi, s) = \sum_{n=0}^{n_{max}} \sum_{m=0}^{n} \widetilde{P}_{nm}(\sin\,\varphi)(a_{nm}\cos(ms) + b_{nm}\sin(ms)) \quad (1)$$

where n_{max} represents the maximum degree of spherical harmonics (in this case, n_{max} = 15), φ is the geocentric latitude of the Ionosphere Piercing Point (IPP), s means the sun−fixed longitude of the IPP ($s = t + \lambda - \pi$), t stands for UTC time, and λ is the longitude of the IPP; $\widetilde{P}_{nm} = \Lambda(n,m)P_{nm}$ are the normalized associated Legendre functions of degree n and order m, based on normalization function $\Lambda(n,m)$ and Legendre functions P_{nm}, a_{nm}, and b_{nm} are the unknown TEC coefficients for spherical harmonics, i.e., the parameters to be determined.

2.1.2. European Space Agency (ESA)

The ESA model, like the CODE model, is based on modeling the TEC values of the ionosphere by using spherical harmonics [22,39] of degree 15 with the assumption of a single layer structure of the ionosphere for an altitude of 450 km and daily differential code biases (DCB) values for receivers and satellites.

2.1.3. Jet Propulsion Laboratory (JPL)

This model uses a three−dimensional approach based on the surface triangulation method by tessellating a sphere at a given height, with TEC values extracted from the vertices of the resulting equilateral triangles [23]. In this case, surface tessellation involves fitting an icosahedron to a sphere of a given radius (in this case, 450 km) so that two nodes align the north and south poles, followed by dividing the resulting equilateral triangles into four smaller ones. This results in 1280 contiguous equilateral triangles. The TEC value between nodes is modeled linearly, while the global distribution of TEC values is obtained using a bidirectional TEC gradient. This model can be represented in the following form:

$$T_{rs} = M_E \sum_{i=A,B,C} W(\theta, \varphi, i)V_i + b_r + b_s \quad (2)$$

where T_{rs} represents the slant delay value between the receiver and the satellite; θ and φ are latitude and longitude, respectively; M_E represents the scaling function as a function of altitude; V_i is the TEC value at vertex A, B, or C represented as index i in the equation; $W(\theta,\varphi,i)$

are the weighted functions for the sphere piercing point; b_r and b_s are the instrumental errors for the receiver and the satellite, respectively.

2.1.4. Polytechnic University of Catalonia (UPC)

This approach uses a tomographic model, relying on phase measurements from ground−based measurement stations on the L_1 and L_2 bands [24]. The first step in determining the electron density is solving the linear geometry−free combination for phase measurements, i.e., $L_I = L_1 - L_2$, detecting cycle slip effects and splitting the signal into smaller parts. Because the phase measurement is based on a continuous phase transfer, all differences are referred to the first determined point (Equation (3)).

$$\frac{\Delta L_I}{\kappa} = \int_{\vec{r}^T(t^T+\tau)}^{\vec{r}_R(t_{R+\tau})} N_e ds - \int_{\vec{r}^T(t^T)}^{\vec{r}_R(t_R)} N_e ds \tag{3}$$

where $\kappa \approx 1.05$ m per $L_I/10^{17}$ electrons m^{-2}, Ne is the electron density, $\vec{r}$ represents the signal path, t means time, $\vec{r}^T$ state for the position of the transmitter T at the moment of signal transmission at time t^T and $\vec{r}_R$ is the position of the receiver at the moment of signal reception at time t_R, τ is the time difference between continuous phases for the transmitter−−receiver pair in seconds. Dividing the surface of the ionosphere into cells with the size of $5^\circ \times 2.5^\circ$ or $10^\circ \times 5^\circ$ and assuming that the value of electron density in it is constant, Equation (3) takes the following form:

$$\frac{\Delta L_I}{\kappa} = \sum_i \sum_j \sum_k (N_e)_{i,j,k} \left[\Delta s_{i,j,k}^{t+\tau} - \Delta s_{i,j,k}^{t} \right] \tag{4}$$

where i, j, k indicates the ionosphere cell, $(N_e)_{i,j,k}$ denotes the electron density in the cell, and $\Delta s_{i,j,k}^t$ is the signal length that is in the cell. This model has better horizontal resolution, while the vertical values are complemented by Low Earth Orbit (LEO) ionosondes measurements. The benefit of using the tomographic method is the elimination of satellite and receiver DCBs and phase indeterminacy, provided there are no gaps in the signal, which is ensured by splitting the signal into smaller parts after detecting the cycle slip effect.

2.1.5. Wuhan University (WHU)

The WHU model, like the CODE and ESA models, is based on spherical harmonics of degree 15; however, to eliminate negative values [25], the inequality−constrained least squares (ICLS) method is implemented. First, areas with negative TEC must be identified by resolving spherical harmonics using the least square approach. Through this, nodes with negative TEC are extracted in a grid of squares spanning -87.5° and 87.5° latitude and -180° and 180° longitude for thirteen 2-h maps for the entire day. The linear complementary problem is then solved together with the use of the parameter q to calibrate the ICLS solution. The previous steps are repeated until all negative values are eliminated.

2.1.6. International GNSS Service (IGS)

IGS maps are created by applying a weighted average on IAAC maps based on weights obtained by evaluating TEC maps using the inverse root mean square of errors on STEC variations [28]. This is done at an evaluation center (currently the UPC center). The process of combining DCBs for receivers and satellites is similar. The next stage is their validation by comparing the received maps to a reliable data source. Such a source are altimetry measurements from TOPEX, Jason−1, Jason−2, Jason−3 missions. As these satellites perform measurements of oceans, where it is difficult to have a permanent GPS/GLONASS receiver, interpolated values are in fact used for map evaluation.

There are two main products that are produced to present the state of the ionosphere: rapid GIMs, which require about one day of preparation, and final GIMs, which are made available about 11 days later. For the purposes of this paper, we will refer to the final

products from each center as codg, esag, igsg, jplg, upcg, whug. In the above list, CAS and EMR products were not mentioned because they did not participate in the study. These two centers began generating maps from 2015, while the data from the other centers was obtained from 2005. We decided to eliminate these two centers from the study to ensure a uniform study period.

2.2. Altimetry TEC

The primary purpose of altimetry satellites is to measure the distance between the satellite and the surface of the oceans with centimeter accuracy. Altimetry measurements began in 1992 with the launch of the TOPEX/Poseidon mission, which lasted until 2006, followed by the Jason−1 (2001–2013) and Jason−2 (2008–2019) missions to replace the older satellites. Each satellite was equipped with a "Poseidon" altimeter [40], a GPS receiver, and the Doppler Orbitography and Radiopositioning Integrated by Satellite (DORIS) system. The use of dual−frequency altimetry measurements (5.3 GHz for C−band and 13.575 GHz for Ku−band), which was designed to negate the influence of ionospheric delay, contributed to the application of these data to study the state of the ionosphere. The mentioned satellites orbit at the same altitude (about 1336 km) with the same value of the inclination angle equal 66°. As these satellites perform vertical measurements, the coordinate of the measurement performed is also the ionosphere piercing point, and it allows the calculation of the vertical value of TEC along the signal path [41,42]:

$$TEC = \frac{f_{Ku}^2 f_C^2}{f_{Ku}^2 - f_C^2} \frac{R_C - R_{Ku}}{k_u} \quad (5)$$

where f_{Ku} and f_C are the frequencies at Ku−band and C−band in GHz, respectively; R_{Ku} and R_C are the distances measured in meters at Ku−band and C−band; and k_u is a constant of 0.403 m GHz^2 TECU^{-1}. Ready TEC values for altimetry missions can be obtained from the OpenADB service (https://openadb.dgfi.tum.de/ (accessed on 22 October 2021)) with a 1Hz resolution.

Jason altimetric measurements provide TEC data up to their orbital altitude, i.e., about 1336 km. In the case of GNSS measurements, the signals pass through the whole ionosphere. Therefore, a direct comparison of Jason TEC with GNSS TEC leads to some uncertainties caused by not including plasmaspheric TEC in Jason's measurements. To avoid this, we complemented the observed Jason TEC values with TEC data derived from the IRI−Plas 2020 model [43,44]. According to the model, TEC values above Jason's satellite orbit are between 0.5–6.2 TECU, with a mean of 1.75 TECU for the analyzed period.

To validate Global Ionospheric Maps (GIMs) from different IAACs, we used data from Jason−1E, Jason−2D, and Jason−3F satellites. Altimetry−derived TEC data are affected by significant noise, which the smoothing process should reduce [45]. For that purpose, we use a 30−s moving average. Next, we resampled one−second measurements to 5−min data to avoid data redundancy. This allows for less computational resource consumption and, at the same time, does not affect the quality of the results. Additionally, 1% of values were negative and were removed from the dataset before applying filtering. To directly compare altimetry and GIM TEC, we interpolated GIMs values at the satellite location using bilinear interpolation around the nearest grid nodes.

Because we used data from different Jason satellites, it was necessary to verify their consistency. Thus, we estimated the bias between the Jason missions. It was possible because the satellites were moving in tandem for a certain period during the launch of the new mission. By matching the dates and coordinates between the missions during the period with a common orbit, it was possible to obtain an average bias between them. Jason−2 and Jason−1 followed each other with a delay of 55 s [46] from June 2008 until mid−February 2009, while the delay between Jason−3 and Jason−2 was 80 s [47] from February 2016 until early October 2016. A bias between Jason−2D and Jason−1E equal to 3.22 ± 2.84 TECU and between Jason−3F and Jason−2D equal to −3.97 ± 2.23 TECU was determined, and then the entire data set was aligned with Jason−3F. The results

of applying this operation are very clearly visible, especially during the transition of individual missions. A similar bias between Jason−2D and Jason−1E was determined by Azpilicueta [48], where their determined bias is about 3.5 TECU. In the case of the bias between Jason−3F and Jason−2D, it is difficult to find a comparison because the magnitude of the bias is directly related to the version of the data on which the calculations are performed. Azpilicueta obtained an offset between Jason−3D and Jason−2D of about 2.5 TECU, while Li [49], estimated bias between Jason−3 and Jason−2 that equals 2.7 TECU, but without information on data versions. The differences between the resulting biases are due to using different versions of Jason−3 data (versions D and F). Version F introduced many changes, which are described in detail in the Jason−3 Products Handbook [50].

Figure 1 presents the course of TEC values acquired from altimeter satellites before (top graph) and after the alignment was applied (bottom graph). As Jason's data is acquired at 1 Hz, the amount of data had to be reduced. The blue color presents data with a 5−minute interval. However, the data is very noisy, which interferes with the interpretation of the data. Therefore, the daily (red) and monthly (black) average TEC values are additionally presented for visualization. The vertical green dashed lines mark the beginning of the data for the new Jason missions. The large noise of Jason's TEC visible in Figure 1 is caused by the high orbital velocity of the satellite (about 7.2 km/s), which causes a significant change in the satellite's position in 5 min and, consequently, a large change in electron content.

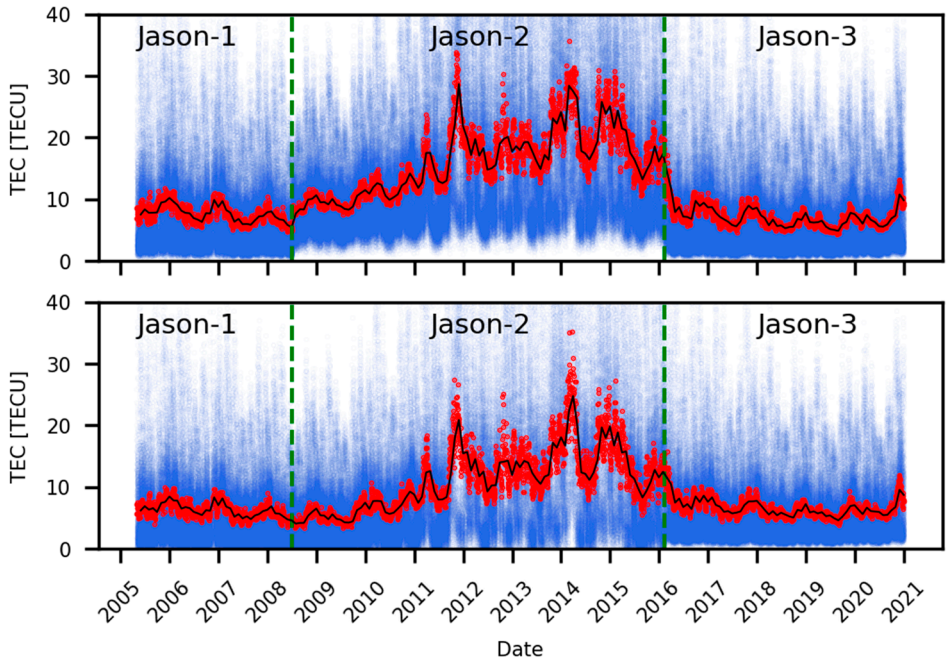

Figure 1. Altimetric−derived TEC data before (**top**) and after application of alignment (**bottom**) to Jason−3F; 5−minute data (blue), daily average TEC (red), monthly average TEC (black).

3. Results

In this section, we analyze differences between the final products from the individual IAAC centers and the TEC derived from the Jason measurements over the years 2005–2020. We present both temporal and spatial analyses from the most general statistics to detailed ones.

When examining the temporal variability of the final products from the IAAC centers and Jason−derived TECs, the differences between them were used, as presented in Figure 2, where the differences for the 5−min interval (blue), daily average (red), and monthly (black) differences for the studied period are shown. The graph compares individual differences to the F10.7 index, representing the degree of solar activity. A clear correlation of differences to the index can be observed, especially for 2011–2016, where an increase in the value of differences and an increase in oscillations can be noted. In addition, it can be observed that

even quiet periods are susceptible to changes in solar activity, as noted by comparing two periods: 2005–2007 and 2019–2021. For the first period, solar activity was higher, which is seen in the values of differences, which are greater than in the second period.

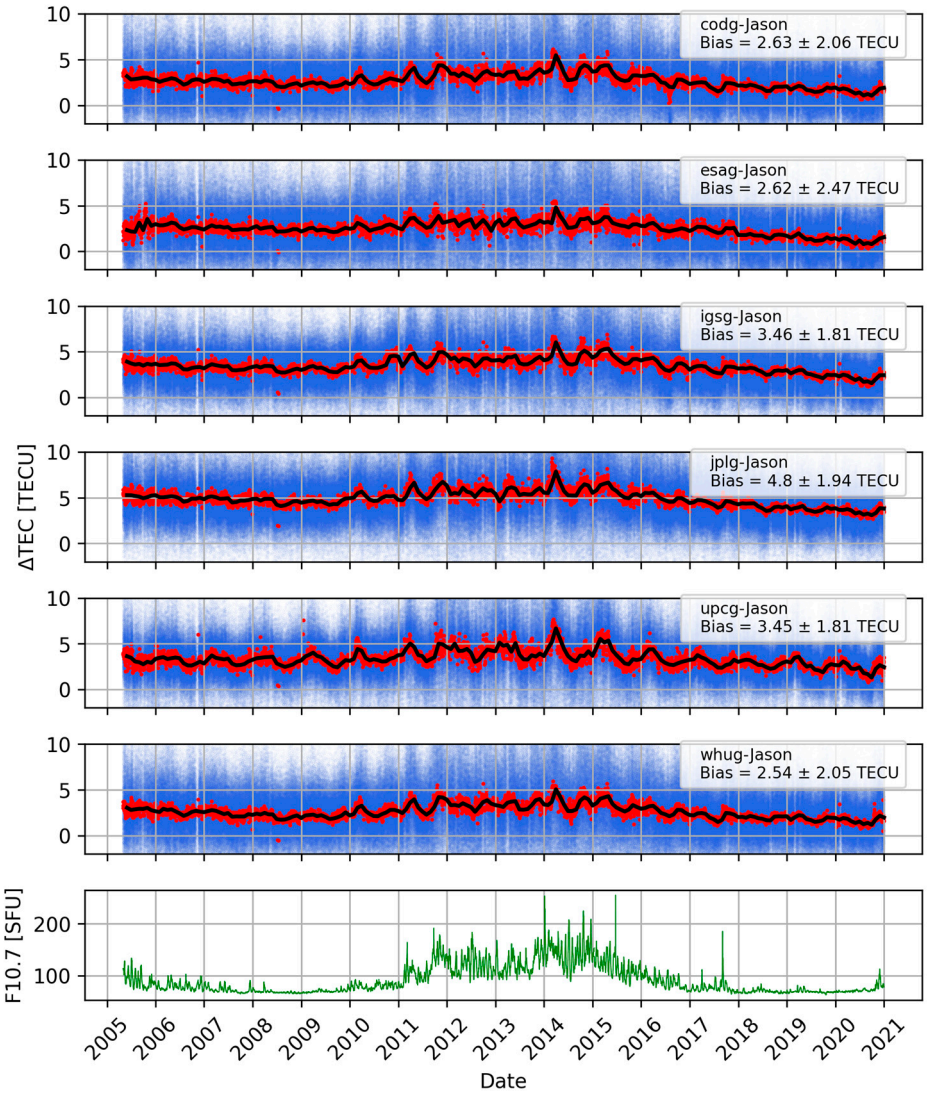

Figure 2. Representation of 5−minute differences (the blue lines) between the final GIMs and the Jason−derived TEC, with comparison to the F10.7 index (the green lines). The red lines represent the daily mean difference, and the black lines show monthly mean difference (From the top: codg-Jason, esag-Jason, igsg-Jason, jplg-Jason, upcg-Jason, whug-Jason, F10.7 index).

The lowest differences were obtained for the codg, esag, and whug models at around 2.6 TECU. Of these three differences, the codg and whug models have a low standard deviation of approximately 2.1 TECU, while for the esag model, it is 2.5 TECU, which is the highest obtained for the six models tested. Of all the differences, the highest bias was received for the jplg-Jason difference of 4.8 TECU with a standard deviation of 1.9 TECU. In contrast, the lowest std was obtained for the igsg and upcg models of 1.8 TECU. However, they have a significant bias of 3.5 TECU. It is worth mentioning that the daily igsg solution comprised 6192 codg and jplg models and 5849 esag and upcg models over the study period. In addition, the esag and upcg solutions never took part in the solution by themselves; whenever they were taken into the calculation, four models took part in the solution. However, the whug model was never considered for the igsg product. In the course of the igsg difference, the influence of almost all the models mentioned above can be observed

except for upcg, which is characterized by an apparent periodicity in the data, making it harder to observe the igsg difference.

As can be noticed, difference values change with changes in solar activity, which occur not only in the average value but also in the dispersion. To better illustrate the problem, in Figure 3 (left), we present differences averaged using a 30-day moving window. The 30-day window for the moving average was chosen to smooth the data without losing major disturbances. Additionally, the 30-day period is close to the rotation period of the Sun (between 27 and 30 days). For codg-Jason, esag-Jason, and whug-Jason, we obtained very similar results, which can be caused by the fact that all of them are generated using spherical harmonics. It can also be observed that the average values of upcg-Jason differences are larger than the others, and an unsimilar course to the others characterizes the course of the average differences itself. We have also noticed a much larger amplitude of fluctuations in the course of the moving average for it. For codg-Jason, esag-Jason, and whug-Jason, we obtained very similar results, which can be caused by the fact that all of them are generated using spherical harmonics. We also observed that the average values of jplg-Jason differences are more significant than the others.

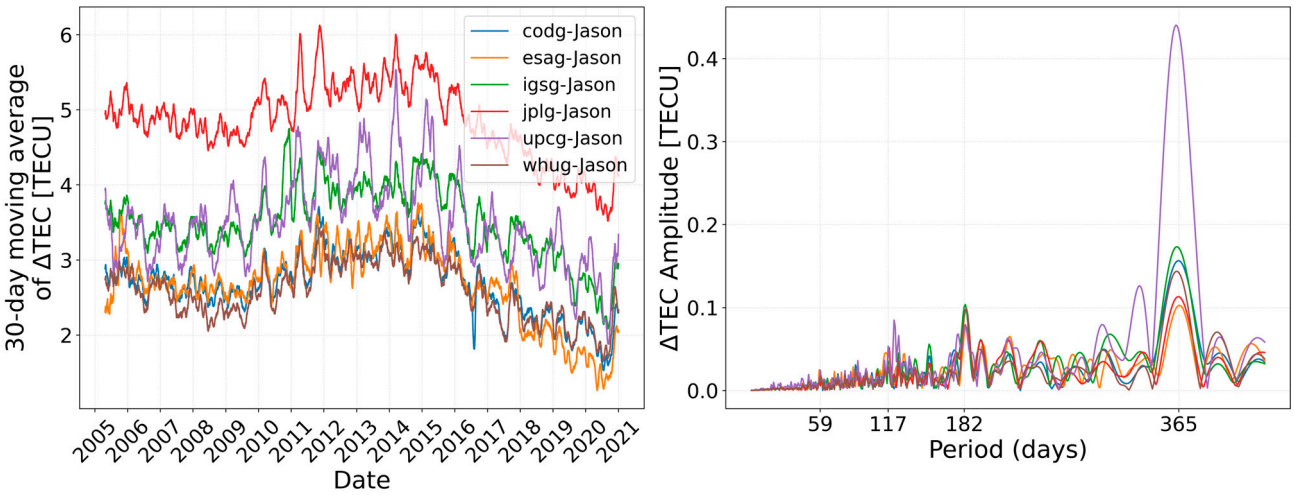

Figure 3. Average TEC differences between IAAC GIMs and Jason−derived data estimated with 30-day moving window (**left**) and Lomb–Scargle periodogram (**right**) for each of them; codg-Jason (blue), esag-Jason (yellow), igsg-Jason (green), jplg-Jason (red), upcg-Jason (purple), whug-Jason (brown).

On the presented results, some periodic changes can also be noticed. After removing the general nonlinear trend (by applying 6−degree polynomial fitting) caused by solar activity, we analyzed the frequency using the Lomb–Scargle method [51,52]. Based on the results presented in Figure 3 (right), we can distinguish two distinct oscillations, annual and semi−annual, which were found for all analyzed cases. Explanations for the appearance of annual and semi−annual oscillations can be found in the literature. Lean [53], in his work, examined the sources of the formation of the annual and semi−annual oscillations. He observed that both cyclicities are mainly related to the intensity of solar radiation and the minor influence of geomagnetic activity. Considering the annual oscillation, it can be deduced that the average showing the highest cyclicity is upcg-Jason, which explains the high amplitude of fluctuations observed in its course. Also, we noted a similar impact of annual variability on codg-Jason, igsg-Jason, and whug-Jason. The least affected by the annual oscillation are the moving averages jplg-Jason and esag-Jason, which can be observed in the smaller amplitudes for the course of these averages. This means that both models reflect this oscillation in a similar way as Jason−derived TEC. The second oscillation observed in the moving average data is semi−annual cyclicity, which is visible

for almost all averages. The exception is upcg-Jason, for which the semi−annual oscillation is weak compared to other models.

Similarly, as for average ΔTEC, we calculate standard deviations with a 30-day window to show how those values changed over time (Figure 4, left). Variations in the standard deviation are directly related to the solar cycle, where we get significantly lower values for the solar minimum period (2007–2009) than for the maximum period (2014), corresponding to the F10.7 index. The codg, igsg, jplg, upcg, and whug models show similar behavior in the time distribution of the standard deviation for periods with lower solar activity. For periods with increased solar activity, we can see that the jplg-Jason and upcg-Jason products deviate from those previously mentioned. A similar problem occurs for igsg-Jason, where we observed a significant difference from the other models since the exit from the solar minimum, where similarity can again be observed after the solar maximum is exceeded. Meanwhile, the most outlier from the other models is esag. The values of the 30-day standard deviation are higher than the others, especially for the 2010–2016 period. When considering the 30-day mean differences, esag-Jason showed one of the smaller mean values, and its temporal distribution was similar to the codg and whug models. However, for standard deviation, we observed significant fluctuations for esag-Jason, the amplitude of which is higher than of the other ones.

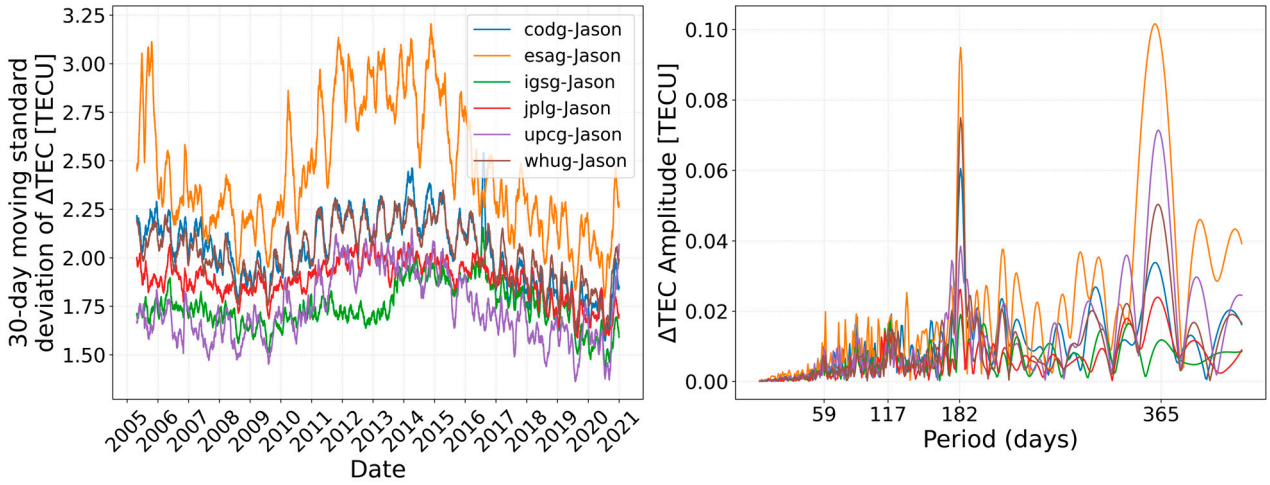

Figure 4. Average standard deviation in differences between IAAC GIMs and Jason−derived data estimated with 30-day moving window (**left**) and Lomb–Scargle periodogram (**right**) for each of them; codg-Jason (blue), esag-Jason (yellow), igsg-Jason (green), jplg-Jason (red), upcg-Jason (purple), whug-Jason (brown).

The Lomb–Scargle periodogram made for this data shows that three oscillations can be identified: annual, semi−annual, and 117-day. In contrast to the results obtained for 30-day mean differences, the half-year oscillation occurring in each of the studied differences is more evident. Considering the oscillation of the 30-day standard deviation, strong subharmonic oscillations can be observed for the annual cyclicity. The largest amplitude for the annual period is exhibited by the esag-Jason difference. Conversely, as anticipated, the igsg-Jason displays the weakest amplitude due to low variation in the differences. Notably, what distinguishes the difference is that the oscillation aligns perfectly with the 365th day, whereas it is shifted a few days back for the others. Regarding the semi−annual oscillation, the highest amplitude is observed for esag-Jason, while the lowest is observed for igsg-Jason. Furthermore, peaks in amplitudes can be observed for differences around days 117 and 59.

To examine the effect of solar activity on changes in the studied models, we checked the correlation between the 30-day averages and their standard deviation against the F10.7 index. As can be observed in the top panel in Figure 5, the bias increases with increased

solar activity. The tested differences maintain a high correlation with the F10.7 index, where the lowest was obtained for the upcg-Jason difference (0.61) and the highest was obtained for whug-Jason (0.79).

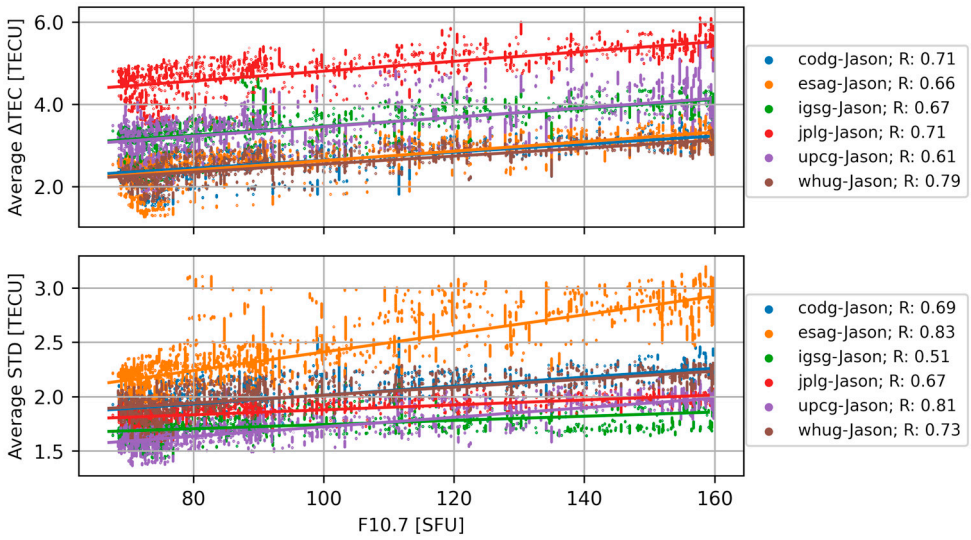

Figure 5. Average TEC differences (**top**) and average standard deviation (**bottom**) in differences between IAAC GIMs and Jason−derived data estimated with a 30-day moving window in comparison to 27-day maximum F10.7 index value; calculated correlations presented in legends; codg-Jason (blue), esag-Jason (yellow), igsg-Jason (green), jplg-Jason (red), upcg-Jason (purple), whug-Jason (brown).

A similar analysis was performed for the standard deviation presented in the bottom panel of Figure 5. It is evident that solar activity has a significant impact on the dispersion of differences. The IGS model is the least vulnerable model to solar activity, whose difference with TEC derived from Jason's measurements obtains the lowest correlation with the F10.7 index (0.51). The highest correlation, on the other hand, is observed for upcg-Jason (0.81) and esag-Jason (0.83) differences. The increase in the standard deviation value is visible for both differences.

We made some spatial analyses for a more detailed analysis of the differences. First, we compute average differences between each of the IAAC GIMs and Jason−derived TEC using a $2^\circ \times 2^\circ$ spatial moving window with the step of 0.5°. For each step, the average difference was estimated based on all data in the specific area and from 2005–2021. As a result, we obtained a spatial distribution of average differences presented in Figure 6. We also counted the standard deviation for each grid node (Figure 7). It is seen that the spatial distribution of the differences is arranged along geomagnetic parallels, with the most significant values taken for intertropical areas and the smallest for the southern hemisphere.

The differences between the codg, esag, whug centers, and Jason−derived TEC particularly stand out due to their high similarity, which is probably due to the use of spherical harmonics in these models. The largest difference values were obtained for jplg-Jason, whose average values in the intertropical zone were 5.6 TECU. High values for this model were also obtained for areas in the northern hemisphere above the Tropic of Cancer (5.1 TECU), where the smallest were observed in the southern hemisphere below the 50°S parallel (3.8 TECU). We noted similar characteristics for other differences. We observed the lowest average values of the differences in the area below 50°S for esag-Jason equal to 1.2 TECU, where codg-Jason and whug-Jason for this area obtained an average of 1.7 TECU. However, comparing the results of these models for the northern hemisphere above 50°N, the values of the previously mentioned differences are close (1.8–2.0 TECU). We conducted a similar analysis for the standard deviation shown in Figure 7. We observed that intertropical areas have the highest average standard deviation from 1.6 (igsg-Jason) to 2.3 (esag-Jason) TECU.

In contrast to the lowest mean differences for the southern hemisphere, the lowest standard deviation was obtained for the northern hemisphere. For all models, the values are similar, ranging between 1.5 and 1.6 TECU. However, for the southern hemisphere below the Tropic of Capricorn, we obtained the highest value for esag-Jason (2.2 TECU). In addition, we noted that for igsg-Jason, the distribution of average standard deviations is uniform across the globe (from 1.5 TECU in the northern hemisphere to 1.6 TECU for intertropical areas and the southern hemisphere).

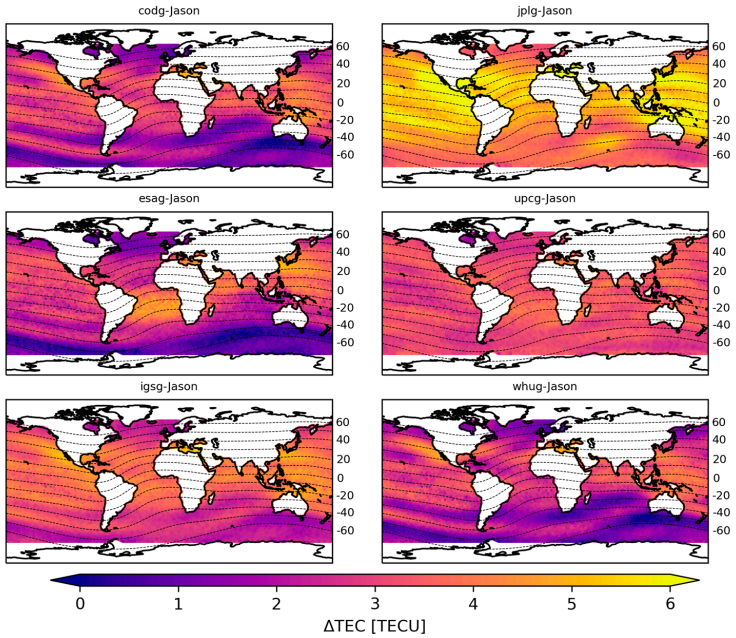

Figure 6. Distribution maps of the moving average of the ΔTEC in the 2° × 2° window with a step of 0.5° for the entire calculation period; (**left**−**top**): codg-Jason, (**left**−**center**): esag-Jason, (**left**−**bottom**): igsg-Jason, (**right**−**top**): jplg-Jason, (**right**−**center**): upcg-Jason, (**right**−**bottom**): whug-Jason. The black dashed lines represent geomagnetic parallels.

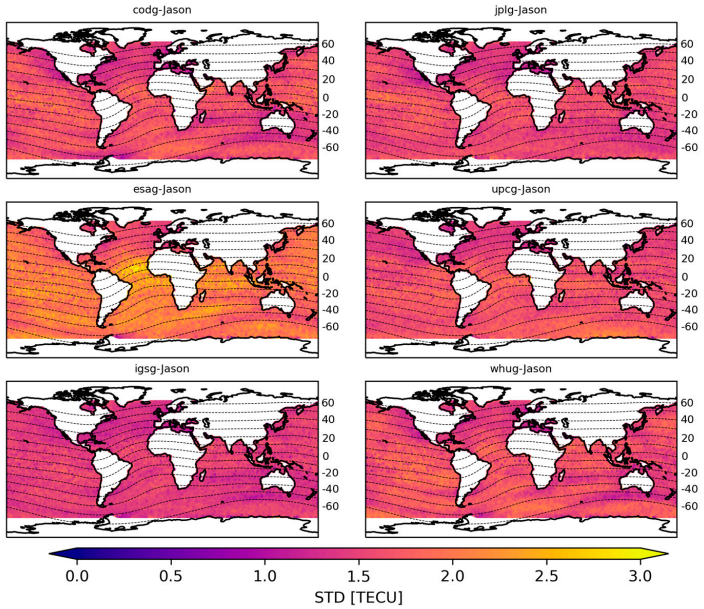

Figure 7. Distribution maps of the moving standard deviation of the ΔTEC in the 2° × 2° window with a step of 0.5° for the entire calculation period; (**left**−**top**): codg−Jason; (**left**−**center**): esag−Jason; (**left**−**bottom**): igsg-Jason; (**right**−**top**): jplg-Jason; (**right**−**center**): upcg-Jason; (**right**−**bottom**): whug-Jason. The black dashed lines represent geomagnetic parallels.

To study the spatial–temporal changes in the differences between individual GIMs and Jason−derived TEC, we performed a quasi−dipole longitude and latitude analysis against local time, shown in Figure 8. The solar cycle is visible in the graphs. A significant increase in the values of differences is observed over the years 2011–2016. The smallest differences are obtained for low or high latitudes, while the largest ones are for intertropical areas. A cyclicity can be clearly observed in the data distribution against geomagnetic latitude, which has a period of about one year. The distribution of differences with respect to quasi−dipole longitude is also characterized by some cyclicity with a period of one year. The dispersion of difference values is regular. However, cyclical decreases in values can be noted for areas from 0° to 120°W and from 120°E to 180°E. It is worth observing that the geomagnetic poles are within both ranges.

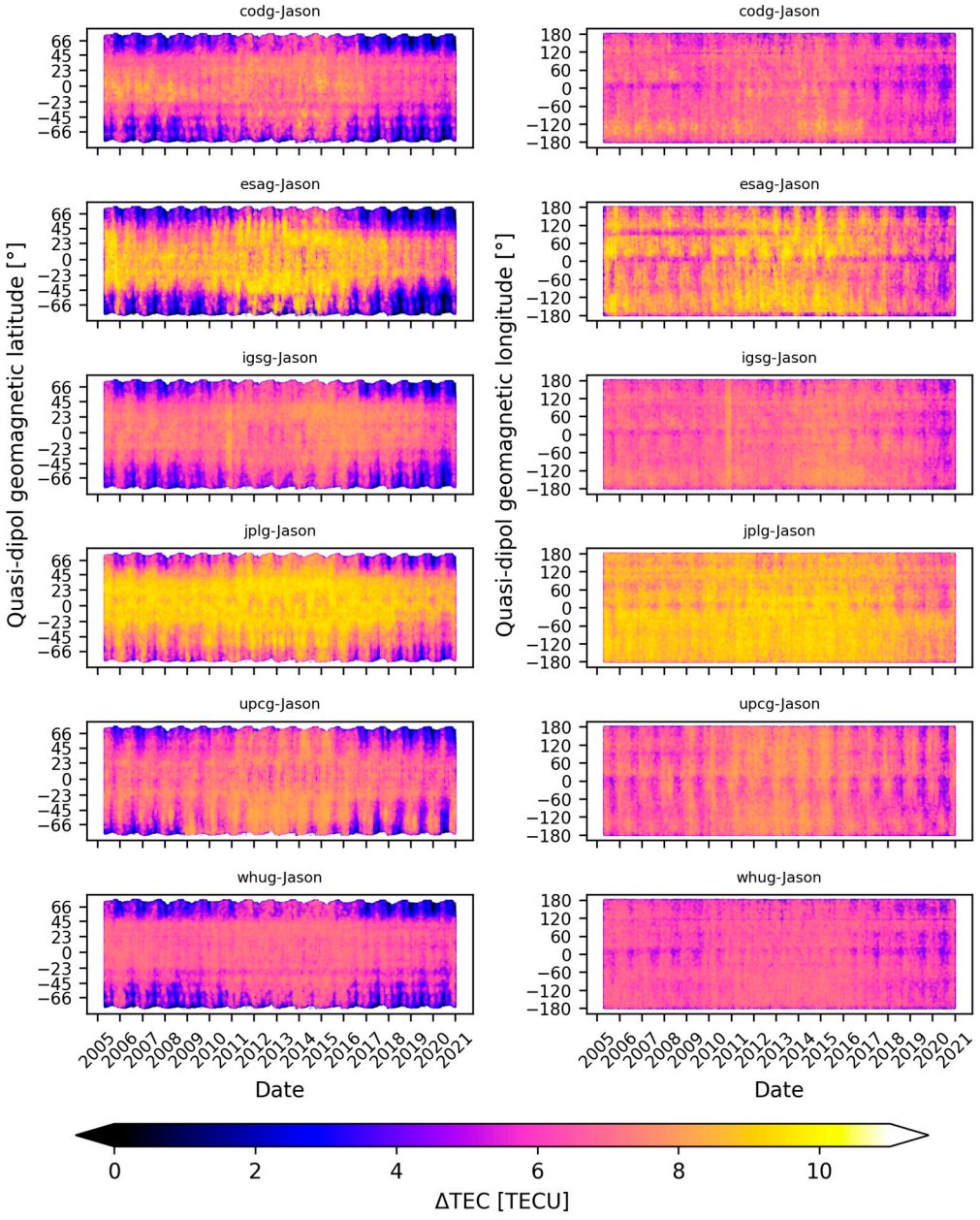

Figure 8. Distribution of differences between GIMs and Jason−derived TEC shown as a function of quasi−dipole geomagnetic latitude (**left column**) and quasi−dipole geomagnetic longitude (**right column**) versus time. From the top: codg-Jason, esag-Jason, igsg-Jason, jplg-Jason, upcg-Jason, whug-Jason.

4. Discussion

Our results indicate a strong correlation between the state of the ionosphere—as represented by GIMs and by Jason−derived VTEC—and solar activity, which is described by the F10.7 index in our study. Obtaining this correlation is not surprising, although we noted that the ratio between VTEC extracted from GIMs and VTEC extracted from altimetry data decreases as solar activity increases. We also investigated how the ratios between individual differences and Jason−derived VTEC or GIMs VTEC look based on periods of low solar activity (2005–2011 and 2016–2021) and high solar activity (2011–2016). The average VTEC differences between GIMs and Jason for this period increased by about 1 TECU for the solar maximum period. Significantly, for the solar maximum period, the ratio between GIMs and Jason data and between individual differences and Jason−derived VTEC decreased by an average of 7% relative to solar minimums, while for differences relative to GIMs, VTEC decreased by 4%. These results can be observed in Figure 9, which shows a comparison between the ratio of GIM to Jason (top), GIM−Jason to Jason (middle), and GIM−Jason to GIM (bottom). Although the diminution of the ratios mentioned above is insignificant, the decreasing ratios may indicate TEC smoothing for increased solar activity by one of the methods.

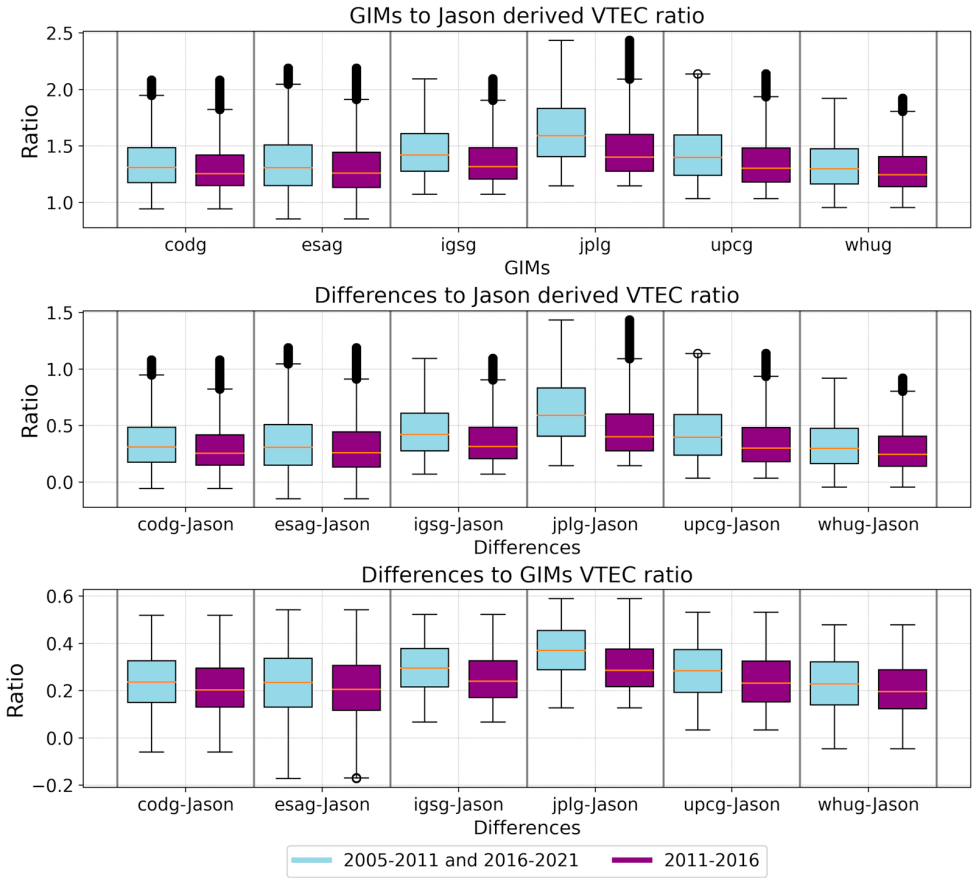

Figure 9. Comparison between the ratio of GIMs to Jason−derived VTEC (**top**), GIMs-Jason VTEC to Jason VTEC (**middle**), and GIM-Jason−derived VTEC to GIMs (**bottom**); the blue box indicates low solar activity periods (2005–2011 and 2016–2021) and the purple box represents high solar activity periods (2011–2016).

In addition to the strong correlation with solar activity, we observed an interesting spatial relationship between GIMs and Jason−derived VTEC. It would be expected that the IGS product (a weighted average product of the other IAAC maps) would show the best match to the VTEC from Jason. The prediction turns out to be confirmed, even though the bias presented in Figure 2 is not the lowest (this is due to the method of creating the

IGS maps). The resulting standard deviation (±1.81 TECU) is the lowest (along with upcg), indicating a better match between the IGS data and JASON despite the higher bias. In addition, we presented the spatial distribution of the moving average and moving standard deviation in Figures 6 and 8. We observed that the moving standard deviation of igsg-Jason has the most even distribution with the smallest standard deviation values among the other differences. As indicated above, the moving average bias is not the lowest, although its spatial distribution is even (similar for upcg-Jason), which cannot be observed in the other maps.

In the process of carrying out the study, in addition to the annual oscillations noted in Figure 8, we also observed the occurrence of semi−annual oscillations and oscillations with a period of about 60 days and 117 days, determined from periodograms using the Lomb–Scargle method, presented in the form of a heatmap in Figure 10.

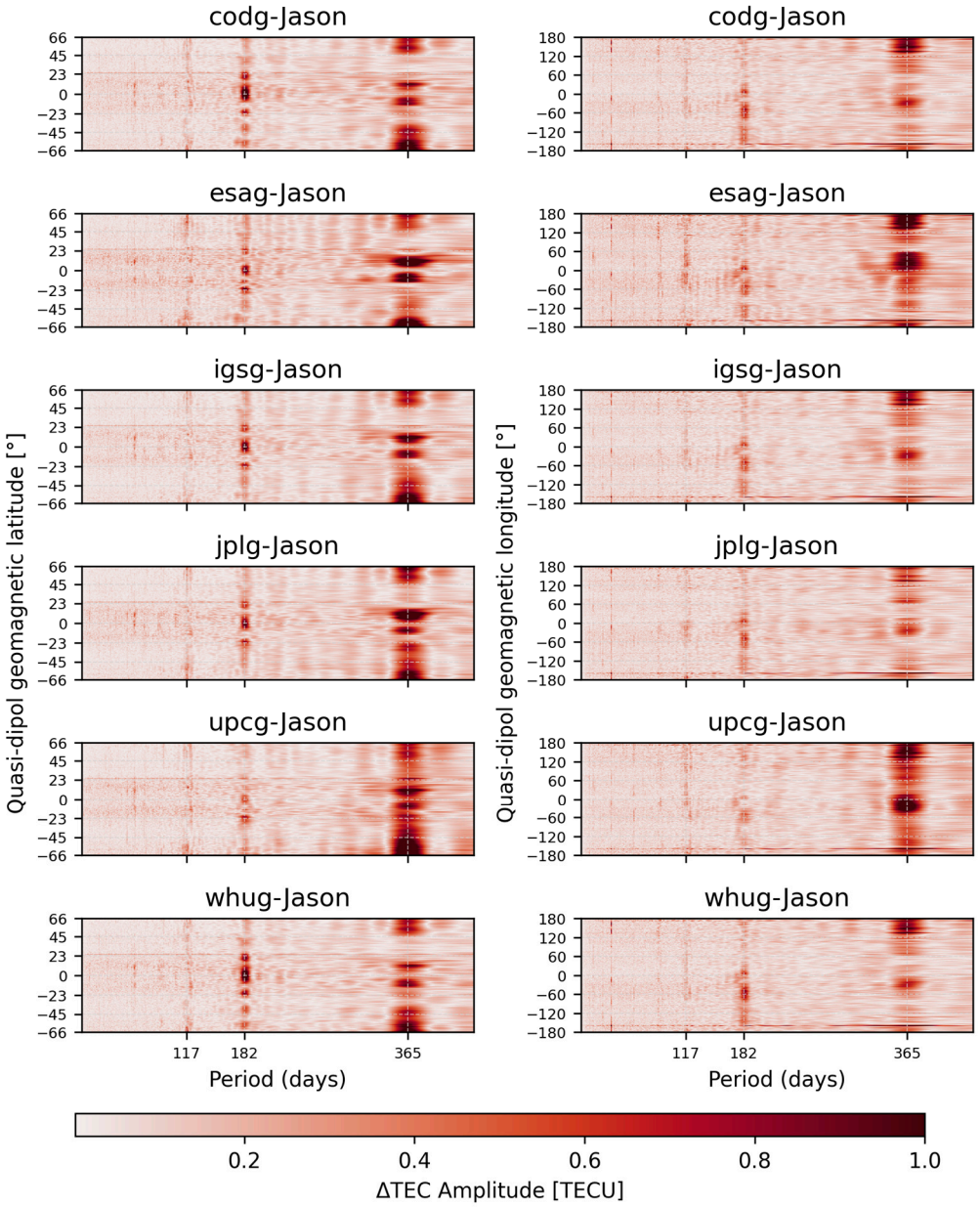

Figure 10. Presentation of oscillation amplitudes in heatmaps as a function of geomagnetic latitude (**left column**) and longitude (**right column**) against the oscillation period for the studied differences. From the top: codg-Jason, esag-Jason, igsg-Jason, jplg-Jason, upcg-Jason, whug-Jason).

We recorded the highest amplitude for the annual and semi−annual oscillations for both longitude and latitude for the studied differences. In both cases, the most pronounced oscillation observed in the data is the annual oscillation that we noted for each of the differences studied. The areas of its occurrence are different for all models. Common regions for which the annual oscillation was noted are areas between 120–180°E for geomagnetic latitudes above 45°N, below 45°S, and around the equator. We noted that for the upcg-Jason data, oscillations related to geomagnetic latitude occur most heavily of all. In addition, apart from the region between 120°–180°E, where particularly strong oscillations were noted, for the upcg-Jason model, we observed a strongly accentuated cyclicity for regions between 60°W and 10°E. In contrast, the semi−annual oscillation calculated concerning geomagnetic latitude occurs mainly for equatorial areas and close to the geographic Tropic of Cancer (23.5°N) and Capricorn (23.5°S). We also noticed that the power of occurrence of this oscillation takes place in the western hemisphere. We observed that the strength of the occurrence of the semi−annual oscillation is similar for most models except for upcg-Jason, for which this oscillation is weakly accentuated, confirming previous analyses for Figure 1. When conducting amplitude analyses of individual oscillations, we noted an additional periodicity, with a 117-day period occurring mostly for geomagnetic latitude. This oscillation is characterized by a greater spatial dispersion of the amplitude of its occurrence, where the highest power was obtained for the polar circle areas. For codg-Jason and whug-Jason, this oscillation is mainly observed for regions below 60°S, while for esag-Jason and igsg-Jason, this oscillation occurs mainly for regions above 50°N.

To perform a more detailed analysis, instead of examining oscillations for the entire globe, we chose a smaller area, from 5°W to 5°E and from 5°S to 5°N. In this area, we have interpolated TEC from GIMs to the position and epoch of Jason. Figure 11 shows the oscillation amplitudes for respective VTEC sources for the study area. We observed that the most pronounced cyclicity is the 117-day period with an amplitude of about 5 TECU, where the amplitude of the semi−annual oscillation reaches up to 4 TECU, while for the annual oscillation, depending on the VTEC source, it is from about 2.5 to 3.8 TECU. In addition, an around 59-day oscillation has become apparent, with an amplitude of up to about 1.5 TECU. It is also worth noting that all studied VTEC sources (individual GIMs and Jason−derived TEC) have the same distinct oscillation periods, indicating a clear connection to the state of the ionosphere rather than the mapping technique or equipment used.

In Figure 11, we observed a very clear 117-day oscillation for the Jason data and for the GIMs data interpolated to the epoch and position of the altimetry measurements. A 117-day periodicity of Jason Doppler Orbitography and Radiopositioning Integrated by Satellite (DORIS) measurements has been reported in the literature [54,55]. This periodicity is called the Jason draconic period, the time that elapses between two flights through the ascending node. This phenomenon is the likely cause of the 117-day oscillation for the Jason−VTEC data. However, the lack of information in the literature on the 117-day periodicity in the ionospheric state forced us to study this phenomenon in more detail. We hypothesized that the interpolation to position and Jason epochs is the reason for such a pronounced oscillation for the GIMs data. To confirm this, we performed a spectral analysis for the ionospheric map data for the map node, which was the center of the study area (0°N, 0°E). This approach enabled us to circumvent the interpolation process, meaning that we retained the identical position and time intervals between samples (2 h).

The results presented in Figure 12 confirm our hypothesis, revealing that interpolating to Jason's position and time contributed to a modification in the cyclicity of the GIMs data. Jason's measurements exhibit a prominent 59-day oscillation, which is a harmonic of the 117-day oscillation [54]. Furthermore, we observed a slight 121-day oscillation that aligns with the GIMs oscillation. Moreover, upon examining a specific map node (in this case 0°N, 0°E), we did not detect a 59-day oscillation; instead, a weak yet distinct peak spanning 27 days was observed, coinciding with the recognized oscillation associated with the rotation of the Sun [56].

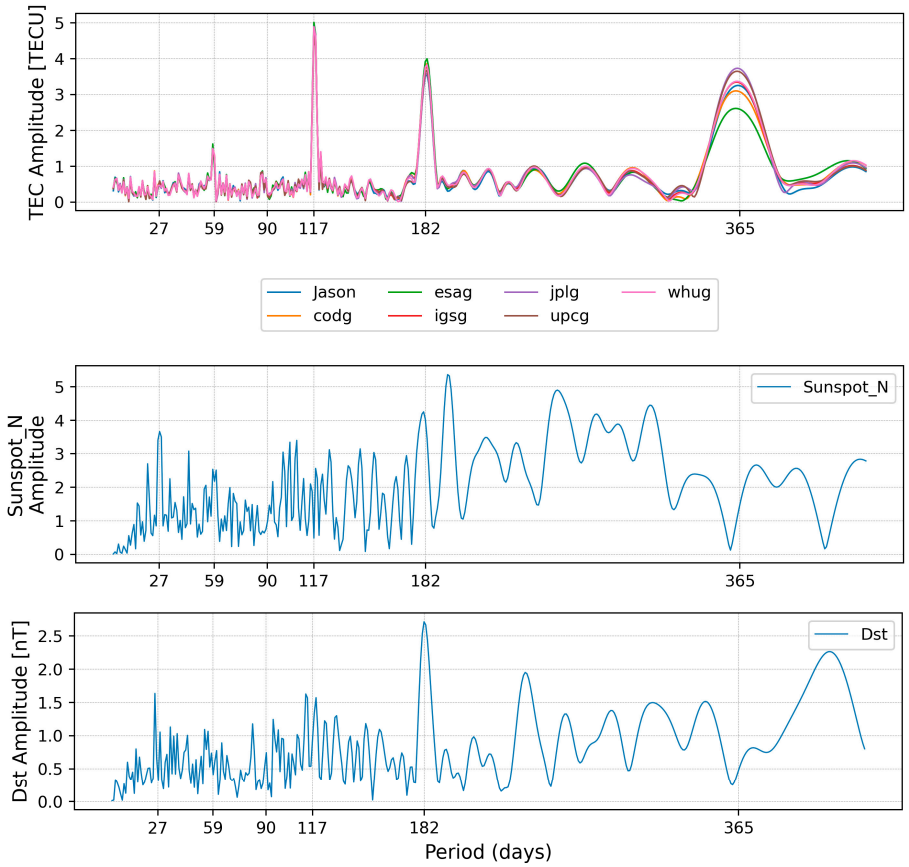

Figure 11. Lomb–Scargle periodogram representing oscillations amplitude for each TEC source (**Top**); Jason (blue), codg (orange) esag (green), igsg (red), jplg (purple), upcg (brown), whug (pink); Lomb–Scargle periodogram for the Sunspot number (**middle**) and for the Dst index (**bottom**).

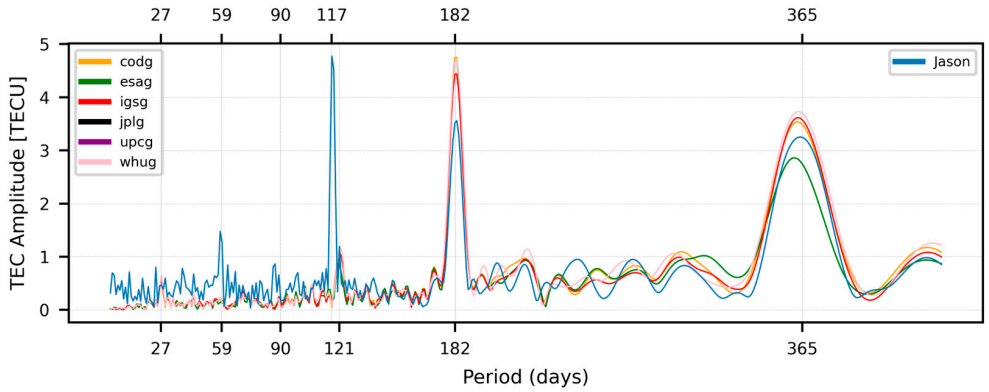

Figure 12. Lomb–Scargle periodogram representing oscillations amplitude for each GIM−TEC in map node (0°N, 0°E) and in 10° × 10° area around studied coordinate for Jason−derived TEC; Jason (blue), codg (orange) esag (green), igsg (red), jplg (purple), upcg (brown), whug (pink).

We checked the probability of false detection to verify whether the obtained oscillations were significant. Based on the results, it has been established that for Jason−VTEC, the annual, semi−annual, and 117-day oscillations are confirmed as significant. However, the cyclicity of approximately 59 days is deemed to be a false one. This is not surprising because this periodicity is a harmonic of the 117-day oscillation. When considering node oscillations for GIMs, the 121-day and 27-day oscillations are both true, along with the annual and semi−annual oscillations. We did not detect a 117-day or 59-day oscillation in the GIMs data.

An intriguing finding arises from the experiment concerning the Dst parameter, which characterizes geomagnetic activity. While studying oscillations for Jason−TEC, we checked amplitudes of Dst index, which is displayed in Figure 11, revealing semi−annual and 27-day peaks in data. The 27-day oscillation is related to the rotation of the Sun [57], which is confirmed by a distinct peak for the sunspot number, which correlates with the peak in the Dst index. The occurrence of a semi−annual peak for Dst is related to the Russell–McPherron effect [58]. We observed that annual and semi−annual oscillations occur in the data, allowing us to conclude that the annual oscillation originates in the annual solar cycle. In contrast, the semi−annual cyclicity depends on both solar and geomagnetic activity. However, we observed that the matter is more complicated for an oscillation of 117 days.

Since the 117-day oscillation occurs only in the Jason data, the source of these oscillations may be related to the measurement technique we described above. In addition, we did not observe clear peaks for this oscillation in the sunspot number and Dst index data. The 117-day oscillation has been documented in the literature. However, these studies do not specifically reference TEC measurements. The 117-day cyclicity in the electron density distribution within the ionosphere has not yet been addressed in scientific literature. Additionally, the puzzling aspect lies in the observation that spatio−temporal interpolation from ionospheric maps to Jason epochs alters oscillatory patterns within the data.

The 120-day oscillation has already been detected in the literature, as presented by Djurovic and Pâquet [59]. They noted a cyclicity of around 120 days for solar activity parameters such as Sunspot Number, Interplanetary Magnetic Field (IMF), Solar Activity index, and some geomagnetic indices. For the sunspot number and the Aa global geomagnetic index they observed an oscillation of about 116 days, and for the solar activity index observed 114 days. In contrast, in our data, we detected a 121-day oscillation for TEC from the GIMs, which is not reflected in the sunspot number and Dst index oscillations. A 120-day oscillation was also detected when studying the neutral winds in the mesosphere and lower thermosphere [60]. This cyclicity was observed in particular for the solar activity described by the F10.7 index and the Lyman−alpha irradiance, indicating the significant influence of solar activity on this oscillation. The failure to detect clear peaks for the indexes studied may be due to the long period of data. In his work, Das used 5 years to study the oscillation, while Djurovic and Pâquet used 9 years. In our work, we study a 16-year period, which includes the 11-year oscillation associated with the solar cycle.

In the same manner as in Figures 11 and 13, we have presented an analysis performed for the differences between the 30-day window moving average for individual GIMs and Jason−derived VTEC. To perform difference analyses, we used VTEC measurements from GIMs interpolated to epochs and Jason's position in a $10^\circ \times 10^\circ$ area around the point under the study. For the differences, the amplitudes reach values at most around 0.4 TECU for the annual oscillation for the upcg-Jason differences. The semi−annual oscillation is much weaker, with amplitudes reaching 0.1 TECU. The 117-day and around 60-day oscillations are very weak but still exist, which is visible when the oscillations associated with the annual cycle are removed. The low amplitude values for the differences mean that the models used to create the GIMs and the VTEC extracted from the altimetry measurements represent the cyclic variability of the ionosphere with similar size. This is related to interpolating ionospheric map data into epochs and Jason's position. The change in oscillations that occurred for the GIMs results in the leveling of these oscillations when considering the differences.

Up to this point, we have discussed oscillations mainly in terms of time, but the problem is also related to spatial location. Not every part of the globe is characterized by the same strength of oscillations. We presented the results of the spatial–temporal analysis in Figure 14. The analysis is similar to Figure 10; however, in this case, we analyzed areas of $10^\circ \times 10^\circ$ around particular latitudes and longitudes. The areas for which amplitude plots were not generated did not reach sufficient data to make them. This is mainly due to the presence of land since, in our study, we used only areas for which altimetric data are available. The Y−axis scale is the same for each graph (from 0 to 6 TECU).

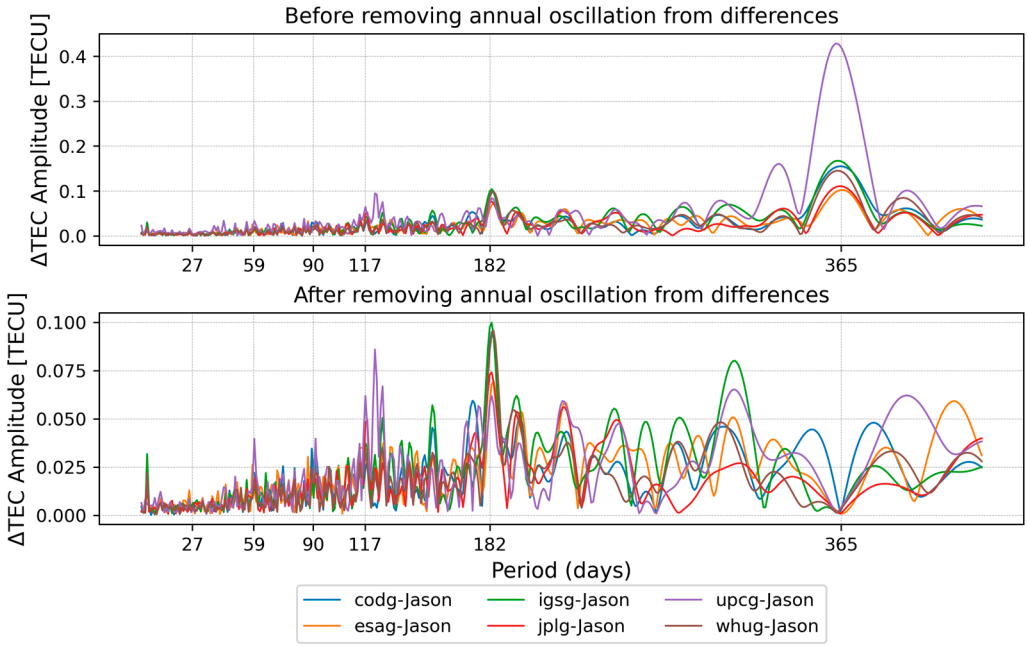

Figure 13. Lomb–Scargle periodogram representing oscillation amplitude for each difference between 30-day moving average and Jason for each GIM before (**top**) and after (**bottom**) removing annual oscillation; codg-Jason (blue) esag-Jason (ornage), igsg-Jason (green), jplg-Jason (red), upcg-Jason (purple), whug-Jason (brown).

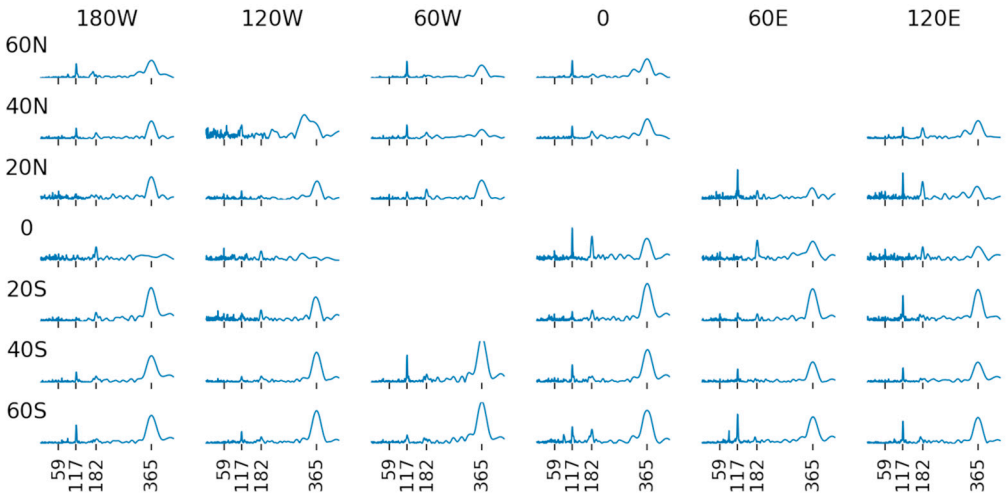

Figure 14. Lomb–Scargle periodogram representing oscillations amplitude for Jason−derived TEC in $10^\circ \times 10^\circ$ areas around studied coordinates.

We observed distinct annual and semi−annual oscillations for most areas. In addition, an oscillation of 117 days occurs over most of the globe, and its amplitude is usually larger or comparable to the semi−annual amplitude. We have not recorded annual oscillation for tropical areas near 120°W and 180°W. We can rule out the lack of data for these areas because they are located in the oceans where Jason's data is available. The semi−annual fluctuations are particularly weak in parts of the Southern Hemisphere east of the zero meridian.

We also checked the spatial distribution of the amplitudes obtained for nodes of the IGSG GIM grid. We selected nodes every 30° in longitude (from 180°W to 180°E) and every 10° in latitude (from 85°N to 85°S). We presented the obtained results in the form of amplitude distribution maps in Figure 15.

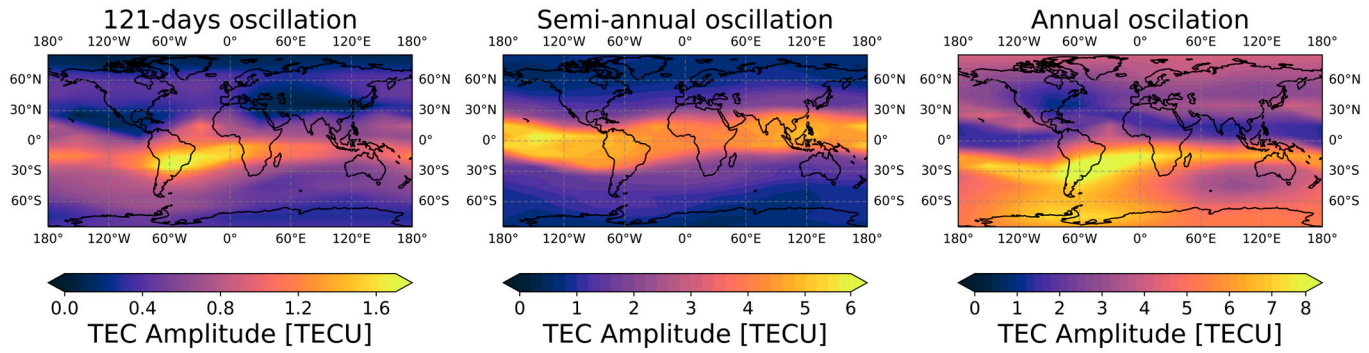

Figure 15. Distribution maps of amplitudes for the selected IGSG GIM grid nodes; 121-day oscillation (**Left**), semi−annual oscillation (**center**), annual oscillation (**right**).

We observed that the 121-day oscillation exhibits relatively low amplitudes compared to the annual and semi−annual oscillations. We observed a distinct correlation between its distribution and the course of geomagnetic coordinates. Furthermore, we found that the highest values of this oscillation are observed near the geomagnetic equator, where the amplitude reaches up to 1.6 TECU. Conversely, the intertropical region is most susceptible to the semi−annual oscillation in TEC values, with amplitudes reaching up to 6 TECU, while they remain relatively weak for the rest of the globe. We noted an interesting phenomenon regarding the annual oscillation, where a clear division between the Earth's hemispheres can be observed. In the southern hemisphere, the GIMs nodes exhibit intense annual oscillations, with amplitudes reaching up to 8 TECU. On the other hand, in the northern hemisphere, the amplitudes are lower, yet the oscillation remains quite pronounced, with amplitudes ranging between 2 and 5 TECU in this area. The results are similar for the other GIMs, so we chose IGSG as a representative example.

5. Conclusions

This paper focused on spatial and temporal differences between data from GIMs and altimetry−derived TEC from 2005–2021, depending on solar and geomagnetic activity. The results of our study allow the spatial–temporal dependencies of TEC to be determined, allowing for a better understanding of the influence of the modeling technique on TEC values. We first determined systematic biases between the different altimetry missions and then aligned the data to Jason−3F. After determining the differences, we examined their course in 5−minute, daily, and monthly differences and compared them to the F10.7 index describing the solar activity. We observed a correlation between the course of differences and the course of the F10.7 index. In addition, we determined the biases for the entire calculation period, through which it can be concluded that the upcg-Jason and igsg-Jason differences have the lowest standard deviation. In comparison, the highest std was obtained for the esag-Jason difference. We also investigated changes in average TEC differences between the GIMs studied and Jason−derived TEC over a 30-day window. The course of the average differences of the CODE, ESA, and WHU models is very similar due to the use of spherical harmonics in their solutions. In addition, we observed some cyclicality in all the differences, which was analyzed based on the Lomb–Scargle method. We noted two strongly accentuated oscillations in the data: an annual one for all studied differences and a semi−annual one, which is very weak for the upcg-Jason difference. We conducted a similar analysis for the 30-day standard deviations in the differences studied. In this case, we also observed annual and semi−annual cyclicities, with the semi−annual oscillation being stronger for standard deviations. In addition, we observed an accentuated 120-day oscillation for GIMs. Its occurrence is probably due to the variations in solar and geomagnetic activity, which has been confirmed in the literature [53,59–61].

To further investigate the distribution of differences, we checked their spatial–temporal distribution for geomagnetic longitude and latitude against time. Based on these analyses,

we noted clear oscillations occurring for both cases, where annual oscillation was most visible. We observed very distinct cyclicities for areas from 0° to 120°W and 120° to 180°E. We also checked the distribution of differences on the map, determining the mean differences and standard deviation in a 2° × 2° window moving with a step of 0.5°. Based on these analyses, we observed that the most significant values were obtained for the intertropical areas, the smallest mean differences for the southern hemisphere, and the minor standard deviation for the northern hemisphere. The smaller standard deviation for the northern hemisphere is possible because most IGS stations are located in this area. However, altimetry measurements do not measure land, thus limiting the number of available data in the northern hemisphere, which is the likely reason for the larger bias. In addition, the standard deviation decreases closer to the land. The opposite is true in the southern hemisphere, where we get more altimetry measurements with fewer IGS stations, so there is a smaller bias and a larger standard deviation. We also discovered that average differences and standard deviation for each model on the map are arranged along the geomagnetic parallels.

Finally, to check the strength of the oscillations occurring in the data against geomagnetic longitude and latitude, we used a Lomb–Scargle periodogram, where amplitudes are presented as heatmaps. We observed some clearly accentuated oscillations: annual, semi−annual, and for Jason−derived TEC, 117-day periodicity, and for GIMs−TEC, 121-day periodicity.

The occurrence of 117-day oscillation in the Jason data is due to the draconic period [54, 55]. The impact of this oscillation on Jason−derived VTEC has not been studied before. We noted that the annual oscillation is much stronger for the southern hemisphere for most of the differences (except for esag-Jason), as confirmed in the paper [50]. In addition, we observed that the semi−annual oscillation is strongest for the Western Hemisphere, where the annual oscillation occurs mainly for a geomagnetic longitude between 120°–180°E. In this paper, we presented spatial and temporal distributions for the differences between individual IAAC GIMs and Jason−derived TECs. This allowed us to detect occurring oscillations in the data. During the analysis, we observed a strong relationship between the occurrence of oscillations and solar and geomagnetic activity. We have also confirmed that the technique of taking measurements may be a direct cause of oscillations, especially altimetry measurements of the state of the ionosphere. However, each global ionospheric map is characterized by the same cyclicities with similar amplitudes. The annual and semi−annual oscillations are common to both Jason and GIM measurements.

Author Contributions: Conceptualization, M.P. and G.N.; methodology, M.P., G.N. and C.B.; software, M.P.; validation, G.N. and C.B.; formal analysis, M.P., G.N. and C.B.; investigation, M.P. and G.N.; resources, M.P.; data curation, M.P.; writing—original draft preparation, M.P.; writing—review and editing, G.N., C.B. and J.S.; visualization, M.P. and G.N.; supervision, G.N., C.B. and J.S.; project administration, G.N.; funding acquisition, G.N. All authors have read and agreed to the published version of the manuscript.

Funding: MP and GN acknowledge support from the Gdańsk University of Technology by the DEC-31/2021/IDUB/I.3.3 grant under the ARGENTUM—"Excellence Initiative—Research University" program. The APC was funded by Gdańsk University of Technology by the DEC-31/2021/IDUB/I.3.3 grant.

Data Availability Statement: Total electron content data derived from the Jason satellites were downloaded from Open Altimeter Database (OpenADB) (https://openadb.dgfi.tum.de/en/ (accessed on 22 October 2021)). GNSS global ionospheric maps were collected from Crustal Dynamic Data Information System (CDDIS) (https://cddis.nasa.gov/ (accessed on 15 October 2021)). The datasets containing TEC differences between Jason-derived TEC and GIMs are available from the corresponding author on reasonable request. The data is not publicly available due to privacy reasons.

Acknowledgments: Calculations were carried out at the Academic Computer Centre in Gdańsk.

Conflicts of Interest: The authors declare no conflict of interest.

References

1. Goodman, J.M. The Ionosphere. In *Space Weather & Telecommunications*; The International Series in Engineering and Computer Science; Springer: Boston, MA, USA, 2005; Volume 782. [CrossRef]
2. *ITU-R P.531-14 (08/2019)*; Ionospheric Propagation Data and Prediction Methods Required for the Design of Satellite Networks and Systems. International Communication Union: Geneva, Switzerland, 2019.
3. Hernández-Pajares, M.; Juan, J.M.; Sanz, J.; Orús, R. Second-order ionospheric term in GPS: Implementation and impact on geodetic estimates. *J. Geophys. Res. Atmos.* **2007**, *112*, B08417. [CrossRef]
4. Cahuasquí, J.A.; Hoque, M.M.; Jakowski, N. Positioning performance of the Neustrelitz total electron content model driven by Galileo Az coefficients. *GPS Solut.* **2022**, *26*, 93. [CrossRef]
5. Nava, B.; Coïsson, P.; Radicella, S. A new version of the NeQuick ionosphere electron density model. *J. Atmos. Sol.-Terr. Phys.* **2008**, *70*, 1856–1862. [CrossRef]
6. Bilitza, D.; Altadill, D.; Truhlik, V.; Shubin, V.; Galkin, I.; Reinisch, B.; Huang, X. International Reference Ionosphere 2016: From ionospheric climate to real-time weather predictions. *Space Weather* **2017**, *15*, 418–429. [CrossRef]
7. Jensen, E.A.; Hick, P.P.; Bisi, M.M.; Jackson, B.V.; Clover, J.; Mulligan, T. Faraday Rotation Response to Coronal Mass Ejection Structure. *Sol. Phys.* **2010**, *265*, 31–48. [CrossRef]
8. Peng, T.; Wang, D.; Jia, X.; Ma, Y. Impact of the Ionosphere and GPS Surveying Caused by Coronal Mass Ejection on May 23 2017. In *China Satellite Navigation Conference (CSNC) 2019 Proceedings*; Sun, J., Yang, C., Yang, Y., Eds.; CSNC 2019, Lecture Notes in Electrical Engineering; Springer: Singapore, 2019; Volume 563. [CrossRef]
9. Zhou, W.; Gu, S.; Ge, M.; Wang, J. Analysis of the Effect of the 06-09-2017 Solar Flare on GNSS Signal and Positioning Performance. In *China Satellite Navigation Conference (CSNC) 2018 Proceedings*; Sun, J., Yang, C., Guo, S., Eds.; CSNC 2018, Lecture Notes in Electrical Engineering; Springer: Singapore, 2018; Volume 498. [CrossRef]
10. Nie, W.; Rovira-Garcia, A.; Li, M.; Fang, Z.; Wang, Y.; Zheng, D.; Xu, T. The Mechanism for GNSS-Based Kinematic Positioning Degradation at High-Latitudes Under the March 2015 Great Storm. *Space Weather* **2022**, *20*, e2022SW003132. [CrossRef]
11. Poniatowski, M.; Nykiel, G. Degradation of Kinematic PPP of GNSS Stations in Central Europe Caused by Medium-Scale Traveling Ionospheric Disturbances during the St. Patrick's Day 2015 Geomagnetic Storm. *Remote Sens.* **2020**, *12*, 3582. [CrossRef]
12. Jacobsen, K.S.; Andalsvik, Y.L. Overview of the 2015 St. Patrick's day storm and its consequences for RTK and PPP positioning in Norway. *J. Space Weather Space Clim.* **2016**, *6*, A9. [CrossRef]
13. Subirana, S.J.; Zornoza, J.M.J.; Hernández-Pajares, M. *GNSS Data Processing, Volume I: Fundamentals and Algorithms*; ESA Communications, ESTEC: Noordwijk, The Netherlands, 2013; ISBN 978-92-9221-886-7.
14. Nykiel, G.; Zanimonskiy, Y.M.; Yampolski, Y.M.; Figurski, M. Efficient Usage of Dense GNSS Networks in Central Europe for the Visualization and Investigation of Ionospheric TEC Variations. *Sensors* **2017**, *17*, 2298. [CrossRef]
15. Ren, X.; Zhang, X.; Xie, W.; Zhang, K.; Yuan, Y.; Li, X. Global Ionospheric Modelling using Multi-GNSS: BeiDou, Galileo, GLONASS and GPS. *Sci. Rep.* **2016**, *6*, 33499. [CrossRef]
16. Zhang, L.; Yao, Y.; Peng, W.; Shan, L.; He, Y.; Kong, J. Real-Time Global Ionospheric Map and Its Application in Single-Frequency Positioning. *Sensors* **2019**, *19*, 1138. [CrossRef] [PubMed]
17. Tomaszewski, D.; Wielgosz, P.; Rapiński, J.; Krypiak-Gregorczyk, A.; Kaźmierczak, R.; Hernández-Pajares, M.; Yang, H.; Orúspérez, R. Assessment of Centre National d'Études Spatiales Real-Time Ionosphere Maps in Instantaneous Precise Real-Time Kinematic Positioning over Medium and Long Baselines. *Sensors* **2020**, *20*, 2293. [CrossRef] [PubMed]
18. Jakowski, N. Ionosphere Monitoring. In *Springer Handbook of Global Navigation Satellite Systems*; Springer International Publishing: Cham, Switzerland, 2017; pp. 1139–1162. [CrossRef]
19. Themens, D.R.; Watson, C.; Žagar, N.; Vasylkevych, S.; Elvidge, S.; McCaffrey, A.; Prikryl, P.; Reid, B.; Wood, A.; Jayachandran, P.T. Global Propagation of Ionospheric Disturbances Associated With the 2022 Tonga Volcanic Eruption. *Geophys. Res. Lett.* **2022**, *49*, e2022GL098158. [CrossRef]
20. Komjathy, A.; Yang, Y.; Meng, X.; Verkhoglyadova, O.; Mannucci, A.J.; Langley, R.B. Review and perspectives: Understanding natural-hazards-generated ionospheric perturbations using GPS measurements and coupled modeling. *Radio Sci.* **2016**, *51*, 951–961. [CrossRef]
21. Schaer, S.; Beutler, G.; Rothacher, M.; Springer, T.A. Daily global ionosphere maps based on GPS carrier phase data routinely produced by the CODE analysis center. In Proceedings of the IGS Analysis Center Workshop, Silver Spring, MA, USA, 19–21 March 1996; pp. 181–192.
22. Feltens, J. Development of a new three-dimensional mathematical ionosphere model at European Space Agency/European Space Operations Centre. *Space Weather* **2007**, *5*, 12002. [CrossRef]
23. Mannucci, A.J.; Wilson, B.D.; Yuan, D.N.; Ho, C.H.; Lindqwister, U.J.; Runge, T.F. A global mapping technique for GPS-derived ionospheric total electron content measurements. *Radio Sci.* **1998**, *33*, 565–582. [CrossRef]
24. Hernández-Pajares, M.; Juan, J.; Sanz, J. New approaches in global ionospheric determination using ground GPS data. *J. Atmos. Sol.-Terr. Phys.* **1999**, *61*, 1237–1247. [CrossRef]
25. Zhang, H.; Xu, P.; Han, W.; Ge, M.; Shi, C. Eliminating negative VTEC in global ionosphere maps using inequality-constrained least squares. *Adv. Space Res.* **2013**, *51*, 988–1000. [CrossRef]

26. Li, Z.; Yuan, Y.; Wang, N.; Hernandez-Pajares, M.; Huo, X. SHPTS: Towards a new method for generating precise global ionospheric TEC map based on spherical harmonic and generalized trigonometric series functions. *J. Geod.* **2015**, *89*, 331–345. [CrossRef]
27. Ghoddousi-Fard, R.; Héroux, P.; Danskin, D.; Boteler, D. Developing a GPS TEC mapping service over Canada. *Space Weather* **2011**, *9*, S06D11. [CrossRef]
28. Hernández-Pajares, M.; Juan, J.M.; Sanz, J.; Orus, R.; Garcia-Rigo, A.; Feltens, J.; Komjathy, A.; Schaer, S.C.; Krankowski, A. The IGS VTEC maps: A reliable source of ionospheric information since 1998. *J. Geod.* **2009**, *83*, 263–275. [CrossRef]
29. Wielgosz, P.; Milanowska, B.; Krypiak-Gregorczyk, A.; Jarmołowski, W. Validation of GNSS-derived global ionosphere maps for different solar activity levels: Case studies for years 2014 and 2018. *GPS Solut.* **2021**, *25*, 103. [CrossRef]
30. Li, M.; Yuan, Y.; Wang, N.; Li, Z.; Huo, X. Performance of various predicted GNSS global ionospheric maps relative to GPS and JASON TEC data. *GPS Solut.* **2018**, *22*, 55. [CrossRef]
31. Roma-Dollase, D.; Hernández-Pajares, M.; Krankowski, A.; Kotulak, K.; Ghoddousi-Fard, R.; Yuan, Y.; Li, Z.; Zhang, H.; Shi, C.; Wang, C.; et al. Consistency of seven different GNSS global ionospheric mapping techniques during one solar cycle. *J. Geod.* **2018**, *92*, 691–706. [CrossRef]
32. Orús, R.; Hernández-Pajares, M.; Juan, J.M.; Sanz, J.; García-Fernández, M. Performance of different TEC models to provide GPS ionospheric corrections. *J. Atmos. Sol.-Terr. Phys.* **2002**, *64*, 2055–2062. [CrossRef]
33. Chen, P.; Liu, H.; Ma, Y.; Zheng, N. Accuracy and consistency of different global ionospheric maps released by IGS ionosphere associate analysis centers. *Adv. Space Res.* **2019**, *65*, 163–174. [CrossRef]
34. Xiang, Y.; Yuan, Y.; Li, Z.; Wang, N. Analysis and validation of different global ionospheric maps (GIMs) over China. *Adv. Space Res.* **2015**, *55*, 199–210. [CrossRef]
35. Azpilicueta, F.; Brunini, C. Analysis of the bias between TOPEX and GPS vTEC determinations. *J. Geod.* **2008**, *83*, 121–127. [CrossRef]
36. Chen, J.; Ren, X.; Zhang, X.; Zhang, J.; Huang, L. Assessment and Validation of Three Ionospheric Models (IRI-2016, NeQuick2, and IGS-GIM) From 2002 to 2018. *Space Weather* **2020**, *18*, e2019SW002422. [CrossRef]
37. Schaer, S.; Gurtner, W.; Feltens, J. IONEX: The IONosphere Map Exchange Format Version 1, 25 February 1998. In Proceedings of the 1998 IGS Analysis Centers Workshop, ESOC, Darmstadt, Germany, 9–11 February 1998; pp. 233–247.
38. Rui, T.; Qin, Z.; Guanwen, H.; Hong, Z. On ionosphere-delay processing methods for single-frequency precise-point positioning. *Geodesy Geodyn.* **2011**, *2*, 71–76. [CrossRef]
39. Feltens, J. Chapman Profile Approach for 3-D Global TEC representation. In Proceedings of the 1998 IGS Analysis Centers Workshop, Darmstadt, Germany, 9–11 February 1998; pp. 285–297.
40. Yasukevich, Y.V.; Afraimovich, L.; Palamarchuk, K.S.; Tatarinov, P.V. Testing of the international reference ionosphere model using the data of dual-frequency satellite altimeters "Topex"/"Poseidon" and "Jason-1". *Radiophys. Quantum Electron.* **2009**, *52*, 341–353. [CrossRef]
41. Brunini, C.; Meza, A.; Bosch, W. Temporal and spatial variability of the bias between TOPEX- and GPS-derived total electron content. *J. Geod.* **2005**, *79*, 175–188. [CrossRef]
42. Scharroo, R.; Smith, W.H.F. A global positioning system-based climatology for the total electron content in the ionosphere. *J. Geophys. Res. Atmos.* **2010**, *115*, A10318. [CrossRef]
43. Sezen, U.; Gulyaeva, T.; Arikan, F. Online computation of International Reference Ionosphere Extended to Plasmasphere (IRI-Plas) model for space weather. *Geod. Geodyn.* **2018**, *9*, 347–357. [CrossRef]
44. Sezen, U.; Gulyaeva, T.L.; Arikan, F. Performance of Solar Proxy Options of IRI-Plas Model for Equinox Seasons. *J. Geophys. Res. Space Phys.* **2018**, *123*, 1441–1456. [CrossRef]
45. Hernández-Pajares, M.; Roma-Dollase, D.; Krankowski, A.; García-Rigo, A.; Orús-Pérez, R. Methodology and consistency of slant and vertical assessments for ionospheric electron content models. *J. Geod.* **2017**, *91*, 1405–1414. [CrossRef]
46. Roinard, H. *Jason-2 Validation and Cross Calibration Activities (Annual Report 2017)*; Contract No 160182-14026/00 Lot 1.6.3, SALP-TP-MA-EA-23186-CLS, Issue 1rev2; EUMETSAT: Darmstadt, Germany, 2018.
47. Roinard, H. *Jason-3 Validation and Cross Calibration Activities (Annual Report 2020)*; Contract No 160182-14026 Lot 1.8.1, SALP-RP-MA-EA-23473-CLS, Issue 1.1; EUMETSAT: Darmstadt, Germany, 2021.
48. Azpilicueta, F.; Nava, B. On the TEC bias of altimeter satellites. *J. Geod.* **2021**, *95*, 114. [CrossRef]
49. Li, Z.; Wang, N.; Liu, A.; Yuan, Y.; Wang, L.; Hernández-Pajares, M.; Krankowski, A.; Yuan, H. Status of CAS global ionospheric maps after the maximum of solar cycle 24. *Satell. Navig.* **2021**, *2*, 19. [CrossRef]
50. *Jason-3 Products Handbook, SALP-MU-M-OP-16118-CN*, 2.1 ed.; EUMETSAT: Darmstadt, Germany, 2021.
51. Lomb, N.R. Least-squares frequency analysis of unequally spaced data. *Astrophys. Space Sci.* **1976**, *39*, 447–462. [CrossRef]
52. Scargle, J.D. Studies in astronomical time series analysis. II—Statistical aspects of spectral analysis of unevenly spaced data. *Astrophys. J.* **1982**, *263*, 835–853. [CrossRef]
53. Lean, J.L.; Meier, R.R.; Picone, J.M.; Emmert, J.T. Ionospheric total electron content: Global and hemispheric climatology. *J. Geophys. Res. Atmos.* **2011**, *116*, A10318. [CrossRef]
54. Bloßfeld, M.; Zeitlhöfler, J.; Rudenko, S.; Dettmering, D. Observation-Based Attitude Realization for Accurate Jason Satellite Orbits and Its Impact on Geodetic and Altimetry Results. *Remote Sens.* **2020**, *12*, 682. [CrossRef]

55. Belli, A.; Zelensky, N.P.; Lemoine, F.G.; Chinn, D.S. Impact of Jason-2/T2L2 Ultra-Stable-Oscillator Frequency Model on DORIS stations coordinates and Earth Orientation Parameters. *Adv. Space Res.* **2020**, *67*, 930–944. [CrossRef]
56. Ma, R.; Xu, J.; Wang, W.; Lei, J. The effect of ∼27 day solar rotation on ionosphericF_2region peak densities (N_mF_2). *J. Geophys. Res. Atmos.* **2012**, *117*, A03303. [CrossRef]
57. Hocke, K. Oscillations of global mean TEC. *J. Geophys. Res. Atmos.* **2008**, *113*, A04302. [CrossRef]
58. Russell, C.T.; McPherron, R.L. Semiannual variation of geomagnetic activity. *J. Geophys. Res. Earth Surf.* **1973**, *78*, 92–108. [CrossRef]
59. Djurovic, D.; Pâquet, P. A 120-day oscillation in the solar activity and geophysical phenomena. *Astron. Astrophys.* **1989**, *218*, 302–306.
60. Das, S.S.; Kumar, K.K.; Ramkumar, G. First observations of quasi 120 day oscillation in Mesospheric winds and temperature: Observations inferred from Meteor Radar. *Radio Sci.* **2013**, *48*, 310–315. [CrossRef]
61. Tang, W.; Xue, X.-H.; Lei, J.; Dou, X.-K. Ionospheric quasi-biennial oscillation in global TEC observations. *J. Atmos. Sol.-Terr. Phys.* **2013**, *107*, 36–41. [CrossRef]